Experimental Mechanics (2019) 59:95–109
https://doi.org/10.1007/s11340-018-00441-8

Hybrid Split Hopkinson Pressure Bar to Identify Impulse-dependent Wave Characteristics of Viscoelastic Phononic Crystals

A. Haque[1] · R.F. Ghachi[2] · W.I. Alnahhal[2] · A. Aref[1] · J. Shim[1]

Received: 15 May 2018 / Accepted: 8 October 2018 / Published online: 1 November 2018

Abstract

There has recently been a rising interest in the nonlinear wave transmission behavior of phononic crystals. However, experimental studies focusing on the nonlinear wave transmission behavior of phononic crystals have been predominantly performed on 1-D granular crystals using customized impact apparatus. In this study, we explore split Hopkinson pressure bar (SHPB) apparatus as a tool to study the nonlinear wave characteristics of a 1-D continuum viscoelastic phononic crystal. In order to resolve experimental challenges relating to signal-to-noise ratios and input impulse magnitudes, we propose a hybrid SHPB system composed of an aluminum input bar and a nylon output bar. For a considered viscoelastic phononic crystal, the application of the hybrid SHPB apparatus enabled us to observe some low transmission frequency zones, which were not identified from the linearly perturbed settings such as the analytical solution and the electrodynamic shaker tests. We further conducted a series of additional FE simulations to ensure the appearance of impulse-dependent low transmission frequency zones of the considered viscoelastic phononic crystal specimen. The additional sets of simulations evidently illustrate the impulse-dependent evolution of wave transmission coefficients, and demonstrate that the impulse-dependent wave transmission behavior can be experimentally investigated by adopting the hybrid SHPB apparatus. Thus, this study shows that the conventional SHPB apparatus can be employed effectively to study the emerging research field of nonlinear wave characteristics of phononic crystals.

Keywords Hybrid SHPB · Impulse-dependent transmission coefficient · Impact excitation · Electrodynamic shaker · Phononic crystals · Finite-strain viscoelastic model

Introduction

Phononic crystals are periodic structures designed to control mechanical waves through Bragg scattering [1, 2]. Under harmonic excitations with infinitesimal deformation, several analyses have shown that they can possess intriguing wave characteristics such as phononic band-gaps [3–6], acoustic diodes [7–9], and acoustic waveguide [10]. Many experimental studies have been conducted to evaluate wave transmission properties of various phononic crystals as well. Using electrodynamic shakers [11–13] or piezoelectric actuators [6, 14, 15], researchers typically apply infinitesimal deformations or small amplitude forces to investigate the wave characteristics of linearly perturbed phononic crystals.

Recently, there has been a rising interest in the nonlinear wave transmission behavior of phononic crystals, and a wide range of numerical studies have been reported. For instance, some researchers introduced nonlinear constitutive relations in discrete lattice models and investigated the evolution of the dispersion relations [16, 17]. In addition, the wave dispersion relation of weakly nonlinear periodic structures was studied in the finite element (FE) framework [18]. The nonlinear characteristics of wave motion in phononic crystals have also been numerically studied by exploring solitary waves in 1-D granular crystals [19, 20]. However, experimental studies regarding the nonlinear wave transmission behavior of phononic crystals have been predominantly performed on only 1-D granular crystals [21–23]. In these experiments, customized impact apparatus was employed to generate solitary waves in a 1-D chain of elastic beads, whose nonlinearity mainly originates from Hertzian contacts. Then, measured solitary waves were analyzed to identify the impulse-

✉ J. Shim
jshim@buffalo.edu

[1] Department of Civil, Structural and Environmental Engineering, University at Buffalo, 240 Ketter Hall, Buffalo, NY 14260, USA

[2] Department of Civil and Architectural Engineering, Qatar University, Doha, Qatar

dependent wave transmission characteristics [24] or tunable phononic band-gaps [3].

In this study, we experimentally investigate the nonlinear wave transmission behavior of a continuum phononic crystal. Note that continuum phononic crystals are commonly composed of metals and polymers to exploit their high impedance mismatch which brings down the intriguing frequencies to the acoustic frequency range [25, 26]. Due to the inherent viscoelastic and damping properties of polymers, electrodynamic shakers or piezoelectric actuators are not applicable to generate sufficiently large excitation to induce nonlinear wave motion in continuum phononic crystals containing polymers. Here, we examine split Hopkinson pressure bar (SHPB) apparatus as a tool to identify the nonlinear wave characteristics of 1-D continuum viscoelastic phononic crystals. We first present the details of a 1-D viscoelastic phononic crystal under investigation in Sec. "Considered Viscoelastic Phononic Crystal and Loading Conditions". Then, Sec. "Harmonic Excitation Analysis and Results" discusses the *impulse-independent* wave transmission characteristics of the viscoelastic phononic crystal by reviewing its analytical dispersions relation and performing base excitation tests with an electrodynamic shaker. This analysis serves as a reference to study on the *impulse-dependent* wave transmission characteristic of the considered viscoelastic phononic crystal. In Sec. "Impact Excitation Analysis and Results", we introduce a new hybrid SHPB system (i.e., metal input bar and polymeric output bar) to resolve experimental challenges relating to low signal-to-noise ratios and input impulse magnitudes. The effectiveness of the hybrid SHPB in studying impulse-dependent wave characteristics is examined by investigating a series of experiments and simulations.

Considered Viscoelastic Phononic Crystal and Loading Conditions

This section describes the details of mechanical properties of constituents adopted for a continuum phononic crystal (i.e., layered composite) under investigation. In addition, it introduces a brief overview of the two dynamic excitation conditions that are explored in this study to experimentally identify the wave transmission behavior of the considered layered composite.

Material, Constitutive Model, and Specimen

We explore here the impulse-dependent wave transmission behavior of a bilayered composite consisting of metal and polymeric material. For metal, we selected aluminum alloy $6061-T6$, which has the mass density $\rho_1 = 2700\ kg/m^3$, the frequency-independent elastic moduli of Young's modulus $E_1 = 70.0\ GPa$, and Poisson's ratio $\nu_1 = 0.33$. For polymeric material, we chose silicone-based rubber (Elite Double 32, Zhermack), whose mass density and Poisson's ratio are found to be $\rho_2 = 1160\ kg/m^3$ and $\nu_2 = 0.495$ from measurements, respectively. This silicone rubber has been adopted by several other researchers [27, 28], and the current investigation considers both the finite-deformation characteristics and viscoelastic properties of the silicon rubber.

Firstly, the finite-deformation characteristics of the silicone rubber were identified by performing quasi-static uniaxial compression tests at the strain rate of $\dot{\varepsilon} = 1 \times 10^{-3}/s$, and the loading-unloading behavior is presented by the green solid line in Fig. 1a. Then, the equilibrium stress-strain path was determined by taking the mid-path of stress-strain curves from the uniaxial loading-unloading tests [29, 30]. The black dotted line in Fig. 1a shows that the constitutive behavior of the equilibrium path is accurately captured by a Yeoh hyperelastic model [31], whose strain energy is:

$$U = \sum_{j=1}^{3}\left[C_{j0}\left[\bar{I}_1-3\right]^j + \frac{1}{D_j}[J-1]^{2j}\right] \tag{1}$$

where $C_{10} = 199.2\ kpa$, $C_{20} = 16.43\ kpa$, $C_{30} = 23.22\ kpa$, and $D_1 = 30.0\ \ GPa^{-1}$, $D_2 = D_3 = 0.0$. Here, $J = det\,(F)$, $\bar{I}_1 = J^{-\frac{2}{3}} tr\left(F^T F\right)$, and $\boldsymbol{F}$ is the deformation gradient. Secondly, the frequency-dependent viscoelastic properties of the silicone rubber were evaluated through dynamic mechanical analysis (DMA) experiments using RSA-G2 Solids Analyzer (TA Instruments) by applying infinitesimal strain. From the experiments, we obtained the complex-valued Young's modulus $\hat{E}_2(\omega) = \hat{E}_2^{'}(\omega) + i\hat{E}_2^{''}(\omega)$, where $\hat{E}_2^{'}$ and $\hat{E}_2^{''}$ denote the storage modulus and the loss modulus, respectively. Figure 1b shows the obtained frequency-dependent viscoelastic moduli within the sonic frequency range (here, up to $16\ kHz$). Note that we use the angular frequency $\omega = 2\pi f$ in the text, but all the graphs are presented in the linear frequency f. In addition, we adopted the generalized Maxwell model to represent the time-dependent behavior of the considered silicon rubber, whose relaxation modulus $E_2(t)$ can be captured by the Prony series [32]:

$$E_2(t) = E_{2,\infty} + \sum_{j=1}^{10} E_j e^{-\frac{t}{\tau_j}} \tag{2}$$

where e is the Euler constant; $E_{2,\infty}$ denotes the equilibrium (quasi-static) modulus; and each viscoelastic branch j is characterized by an elastic modulus E_j and a relaxation time τ_j. A rheological tool kit (IRIS [33]) was adopted to identify the elastic equilibrium modulus $E_{2,\infty} = 1.196\ MPa$ and the Prony series coefficients E_j and τ_j (see Table 1). The black dotted line in Fig. 1c shows the resulting relaxation modulus $E_2(t)$ at infinitesimal strains. In the time-domain FE simulations presented in Sec. "3 and 4", we adopted the so-called finite-strain viscoelastic model [34, 35], where the infinitesimal-strain equilibrium modulus $E_{2,\infty}$ in (2) is

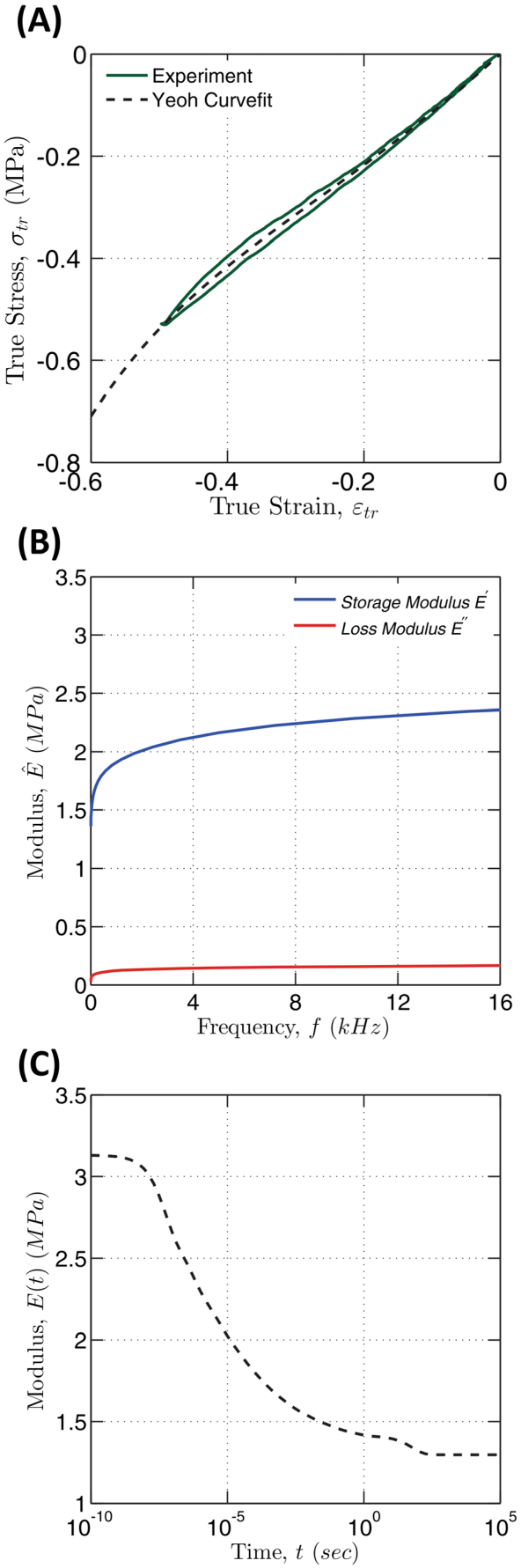

◀ **Fig. 1** Viscoelastic properties of the considered silicone rubber. **a** Loading-unloading stress-strain relation, whose equilibrium path is captured by the Yeoh model. **b** Frequency dependent storage modulus $\hat{E}'(\omega)$ and loss modulus $\hat{E}''(\omega)$. **c** Time dependent relaxation modulus

replaced by the tangent modulus determined by the Yeoh hyperelastic model in (1). All the numerical simulations in this study were performed using a commercial FE software ABAQUS [36], where the finite-strain viscoelastic model is built-in.

The considered bilayered composite specimen was composed of three unit-cells of aluminum ($d_1 = 5\ mm$) and silicone rubber layers ($d_1 = 20\ mm$). The cylindrical specimen had the diameter of 45 *mm* and the overall height of 80 *mm* (see Fig. 2a), and the identical specimen was employed for both shaker and SHPB tests in Sec. "3 and 4". Note that the specimen dimensions (i.e., the thickness and the number of unit-cells) were guided by the analytical study in Sec. "Harmonic Excitation Analysis and Results", so that we could experimentally observe multiple low-transmission zones in the sonic frequency range, which could be achieved by an electrodynamic shaker and SHPB apparatus in the lab.

Consideration of External Excitations

Assuming linear wave motion with infinitesimal deformation, the dispersion relation of phononic crystals composed of dissipative medium is commonly characterized by two experimental approaches: driven-wave or free-wave conditions. While steady-state harmonic oscillations are typically adopted for driven-wave conditions [37, 38], pulse-type loading (e.g., small force excitation or small deformation) is exerted to phononic crystals for free-wave conditions [39, 40]. For the conditions of infinitesimal deformation, the dispersion relations obtained from driven-wave and free-wave conditions are found to be similar for phononic crystals having low damping [41].

Our interest is to investigate impulse-dependent wave transmission behavior of viscoelastic phononic crystals. As a

Table 1 Prony series coefficients of the considered silicone rubber

Branch Number, j	Moduli, $E_j[MPa]$	Relaxation Times, $\tau_j[s]$
1	0.477	4.99×10^{-8}
2	0.328	4.83×10^{-7}
3	0.221	3.55×10^{-6}
4	0.157	1.72×10^{-5}
5	0.113	6.04×10^{-5}
6	0.127	2.28×10^{-4}
7	0.114	1.33×10^{-3}
8	0.077	9.07×10^{-3}
9	0.059	6.42×10^{-2}
10	0.043	4.89×10^{-1}

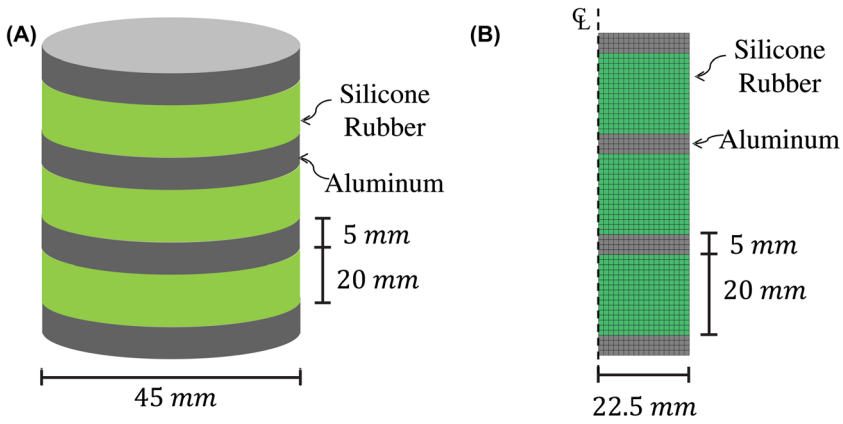

Fig. 2 **a** Geometry of the considered phononic crystal specimen. **b** The corresponding axisymmetric FE model, whose symmetric center-line is denoted by the dotted line

reference study, we first conducted harmonic base excitation tests using an electrodynamic shaker, which generates a voltage chirp signal in the sonic frequency range. The applied forces acting on the considered specimen were small, and consequently the corresponding deformations were infinitesimal. Section "Harmonic Excitation Analysis and Results" presents theses harmonic base excitation test results and the corresponding time-domain FE analysis. Subsequently, the impulse-dependent wave transmission behavior of viscoelastic phononic crystals was investigated by using SHPB apparatus, which allows high impact excitation with nonlinear wave motion in the specimen. Under compressive impact conditions, the silicone rubber layers of the specimen were not in the linear range, showing up to the strain level of $\varepsilon_{tr} = -0.5$. Section "Impact Excitation Analysis and Results" discusses the experimental results from impact excitation with SHPB and the corresponding time-domain FE simulation results.

Harmonic Excitation Analysis and Results

This section discusses the harmonic base excitation conditions inducing only small deformation in the considered layered composite specimen, and the results serve as a reference to the study on impulse-dependent wave transmission characteristics discussed in Sec. "Impact Excitation Analysis and Results". We firstly review the analytical dispersion relation of waves perpendicular to the layers in *infinitely periodic* viscoelastic layered composites, whose detailed derivations can be found in references [42–44]. Then, we describe the details of experimental study using an electrodynamic shaker and the corresponding time-domain FE simulations.

Analytical Dispersion Relation and Transmission Coefficient

As described in Sec. "Material, Constitutive Model, and Specimen", we consider a bilayered composite consisting of alternating viscoelastic and elastic solids. By solving the governing equation of motion together with Bloch periodic boundary conditions [45], we can simultaneously obtain two decoupled eigenvalue problems for dilatational and distortional waves. Here, we focus on dilatational wave motion since compressive waves are mainly considered in the experiments designed in this study. The subscript j is employed to refer the characteristics of the j-th layer (i.e., $j = 1$ for the aluminum layer and $j = 2$ for the silicone rubber layer). For instance, the periodic unit-cell length a is determined by $a = d_1 + d_2$, where d_j is the j-th layer thickness. Assuming steady-state harmonic wave motion in the composite, we can obtain the displacement field $\overline{u}_{j,n}$ and the normal stress field $\overline{\sigma}_{j,n}$ of compressive plane waves for the j-th layer in the n-th unit cell [42]:

$$\begin{aligned}\overline{u}_{j,n}(x_{j,n}) &= P_{F,j,n}e^{-i\frac{\omega x_{j,n}}{c_{p,j}}} + P_{B,j,n}e^{-i\frac{\omega x_{j,n}}{c_{p,j}}},\\ \overline{\sigma}_{j,n}(x_{j,n}) &= -P_{F,j,n}\omega\rho_j c_{p,j}e^{-i\frac{\omega x_{j,n}}{c_{p,j}}} + P_{B,j,n}\omega\rho_j c_{p,j}e^{-i\frac{\omega x_{j,n}}{c_{p,j}}}\end{aligned} \tag{3}$$

where $x_{j,\,n}$ represents the local x−coordinate for the j-th layer in n-th unit cell; $P_{F,\,j,\,n}$ and $P_{B,\,j,\,n}$ are the frequency-dependent complex displacement amplitude to be determined form boundary conditions; $c_{p,j}(\omega) = \sqrt{\frac{\hat{E}(\omega)[1-\nu]}{\rho[1+\nu][1-2\nu]}}$ is the frequency-dependent dilatational wave velocity. By applying the successive stress and displacement boundary conditions at the interfaces, we can obtain the following relation between the complex-valued displacements amplitude vector $\boldsymbol{W}$ of adjacent unit-cells:

$$W_{1,n+1} = TW_{1,n} \tag{4}$$

where

$$W_{1,n} = \begin{bmatrix} P_{F,j,n} \\ P_{B,j,n} \end{bmatrix}, \quad W_{1,n+1} = \begin{bmatrix} P_{F,j,n+1} \\ P_{B,j,n+1} \end{bmatrix} \tag{5}$$

$$T = R_1^{-1}R_2D_2R_2^{-1}R_1D_1 \tag{6}$$

$$R_j = \begin{bmatrix} 1 & 1 \\ -\omega\rho_j c_{p,j} & \omega\rho_j c_{p,j} \end{bmatrix}, \quad D_j = \begin{bmatrix} e^{-i\frac{\omega x_{j,n}}{c_{p,j}}} & 0 \\ 0 & e^{i\frac{\omega x_{j,n}}{c_{p,j}}} \end{bmatrix} \tag{7}$$

Here, $\boldsymbol{T}$ is the frequency-dependent transfer matrix for dilatational wave motion perpendicular to the layers and determines the relation between the displacement amplitude vectors of adjacent unit-cells. In addition to the continuous stress/displacement boundary conditions (4), we have the Bloch periodic boundary conditions between adjacent unit-cells [45]:

$$W_{1,n+1} = e^{i\kappa_{pc}a} W_{1,n} \tag{8}$$

where $\kappa_{pc} = \kappa_{pc}^R + i\kappa_{pc}^I$ is the complex-valued wavenumber of the considered phononic crystals in the direction perpendicular to the layers. While κ_{pc}^R describes the phase of wave propagation, κ_{pc}^I is relating to the amplitude of wave attenuation. The application of Bloch periodic boundary conditions (8) to (4) provides an eigenvalue problem for dilatational wave motion:

$$TW_{1,n} = e^{i\kappa_{pc}a} W_{1,n} \tag{9}$$

By solving the above eigenvalue problem (9), we obtain the frequency-dependent dispersion relations of the considered viscoelastic/elastic bilayered composite for dilatational wave motion perpendicular to the layers [42–44]:

$$\cos(\kappa_{pc}a) = cos\left(\frac{\omega d_1}{c_{p,1}}\right) cos\left(\frac{\omega d_2}{c_{p,2}}\right) - \frac{1}{2}\left(\frac{\rho_1 c_{p,1}}{\rho_2 c_{p,2}} + \frac{\rho_2 c_{p,2}}{\rho_1 c_{p,1}}\right) sin\left(\frac{\omega d_1}{c_{p,1}}\right) sin\left(\frac{\omega d_2}{c_{p,2}}\right) \tag{10}$$

For the considered viscoelastic phononic crystals, the analytical dispersion relation (10) illustrates the characteristics of wave propagation $\left(\omega\text{–}\kappa_{pc}^R\right)$ and wave attenuation $\left(\omega\text{–}\kappa_{pc}^I\right)$, which are shown in Fig. 3a and b, respectively. Unlike in elastic phononic crystals, Fig. 3b illustrates the absence of $\kappa_{pc}^I = 0$ and $d\omega/d\kappa_{pc}^R = \infty$, which indicates that waves in the considered viscoelastic-elastic phononic crystals possesses neither absolute band-gap nor absolute passing-band due to the frequency-dependent dilatational wave velocity of the silicon rubber $c_{p,\,2}(\omega)$. In other words, waves in viscoelastic phononic crystals simultaneously propagate and attenuate at all frequencies.

Here, we introduce a wave transmission coefficient $C_t(\omega)$ by taking the amplitude ratio between input force spectrum $F_{in}(\omega)$ and output acceleration spectrum $A_{out}(\omega)$:

$$C_t(\omega) = \frac{\|A_{out}(\omega)\|}{\|F_{in}(\omega)\|} \tag{11}$$

where $\|\square\|$ denotes the Euclidean norm. Then, the wave transmission coefficient based on the analytical dispersion relation reads:

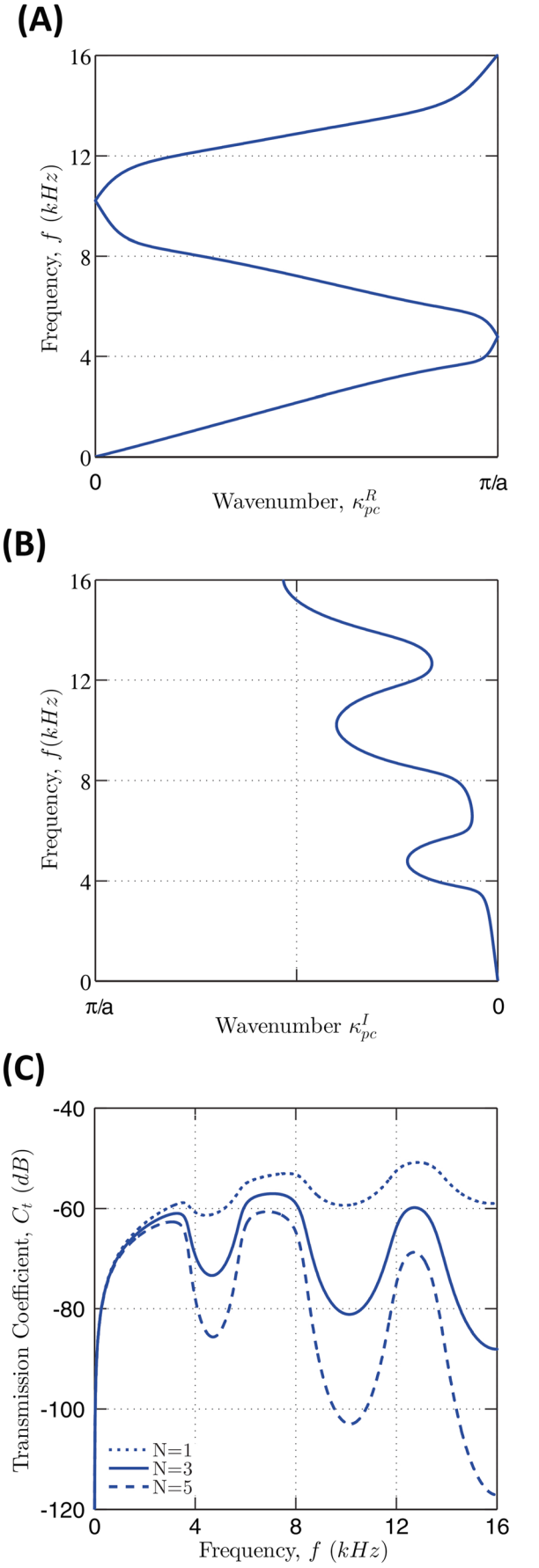

Fig. 3 Pressure wave characteristics of the infinitely periodic viscoelastic-elastic phononic crystal under consideration. **a** Phase dispersion relation, κ_{pc}^R–f. **b** Attenuation relation, κ_{pc}^I–f. **c** Transmission coefficient C_t obtained from (11)

$$C_t(\omega) = \frac{\omega^2 W_{1,n} + N}{\omega \rho_1 c_{p,1} W_{1,n}} = \frac{\omega}{\rho_1 c_{p,1}} e^{-i\kappa_{pc} Na} \tag{12}$$

where the denominator signifies the force vector acting on the aluminum layer in n-th unit-cell and the numerator represents the acceleration vector of aluminum layer in $(n+N)$-th unit-cell. The analytical transmission coefficients for three different unit-cell spacings ($N = 1, 3, 5$) are shown in Fig. 3c, where the coefficient magnitude is presented in dB, i.e., $20log_{10}(C_t)$. As shown in Fig. 3c, the magnitude of the transmission coefficient C_t is affected by N, but the frequency-zones indicating the low transmission are hardly affected by N. In the considered sonic frequency range, we observed three low-transmission frequency zones: first zone around 5 kHz, second zone around 10 kHz, and third zone around 16 kHz. As discussed in Sec. "Material, Constitutive Model, and Specimen", we chose $N = 3$ to design the specimens used in this study.

Base Excitation Tests with Electrodynamic Shaker

Electrodynamic shakers are commonly employed to conduct experiments for low amplitude dynamic excitation. By sweeping frequencies (i.e., chirp signal) through shakers, many researchers have investigated wave transmission characteristics of various periodic structures [11–13]. Figure 4a shows the harmonic excitation test set-up, where an electrodynamic shaker (B&K vibration exciter 4809) was anchored on an optical table. A force transducer (B&K 8230) was assembled to the shaker, and the layered composite specimen was vertically mounted on top of the force transducer. Then, an accelerometer (B&K 4394) was attached at top of the specimen. Swept-frequency chirp voltage signal (up to 16 kHz for 1 s) produced by a waveform generator (NI PXI-5412 with B&K amplifier 2718) was sent to the electrodynamic shaker. Both the force and acceleration time-history measurements were collected at a sampling rate of 1 MHz by a data acquisition system (NI PXI-5105 in NI PXI-1042Q).

The electrodynamic shaker tests were conducted for two different maximum force levels: one with 21.0 N and the other with 53.7 N. By taking the fast Fourier transform (FFT) of the input force acting on the specimen bottom and the output acceleration on the specimen top, we calculated the wave transmission coefficient $C_t(\omega)$ defined in (11). Figure 5A-1 and A-2 show the experimental transmission coefficient spectra $C_t(\omega)$ for the maximum force levels of 21.0 N and 53.7 N, respectively. Note that the force level of 53.7 N was obtained by applying a voltage level close to the specification limit of the electrodynamic shaker. The solid lines in Fig. 5a represent the average of five tests for each force level, and the shaded area along the solid line shows the corresponding standard deviation. From Fig. 5a, we observe three low transmission frequency zones: first zone around 2 kHz, second zone around 10 kHz, and third zone around 14 kHz. Although the electrodynamic shaker tests considered the finite-size layered composite specimen under transient harmonic excitations, the experimentally obtained low transmission zones are found to be in the vicinity of the analytical predictions based on infinitely periodic phononic crystals under steady-state harmonic excitations. More importantly, the comparison between Fig. 5A-1 and A-2 confirms that the experimentally-obtained transmission coefficient spectra are nearly independent of the amplitude of excitation forces generated by the electrodynamic shaker.

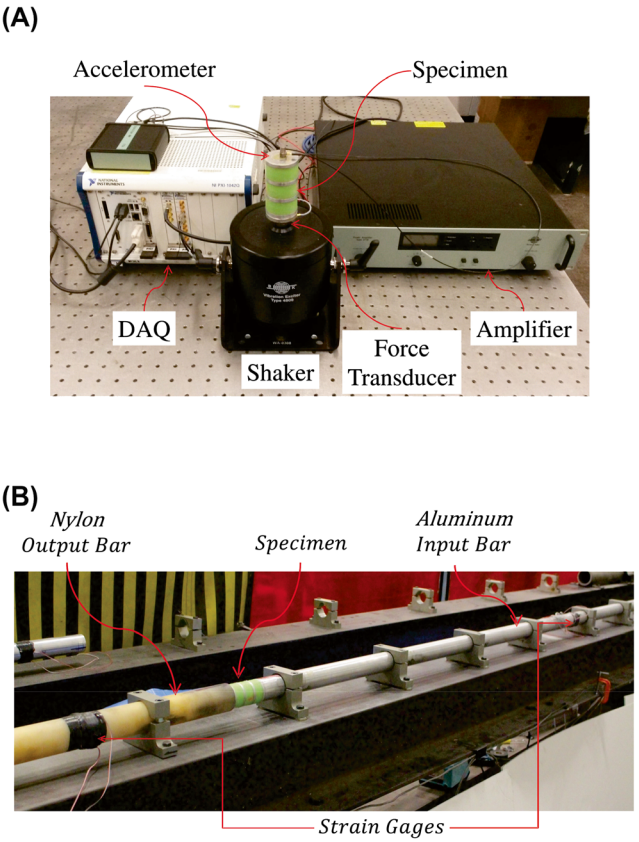

Fig. 4 **a** Electrodynamic shaker test set-up. **b** SHPB test set-up

Time-Domain FE Simulations

For the base excitation tests with the electrodynamic shaker, we also conducted time-domain simulations using the commercial FE code ABAQUS/Standard. All the numerical simulations were performed using a 2-D axisymmetric model with 4-node bilinear element *CAX4R*. A mesh refinement study confirmed that the mesh sweeping size of 1.25 mm (see Fig. 2b) is sufficiently small to obtain the convergence of the FE simulation results. In order to minimize the overall drift of the specimen displacement, we applied an equivalent base acceleration with the baseline correction procedure [46, 47], instead of using the direct force time-history measured

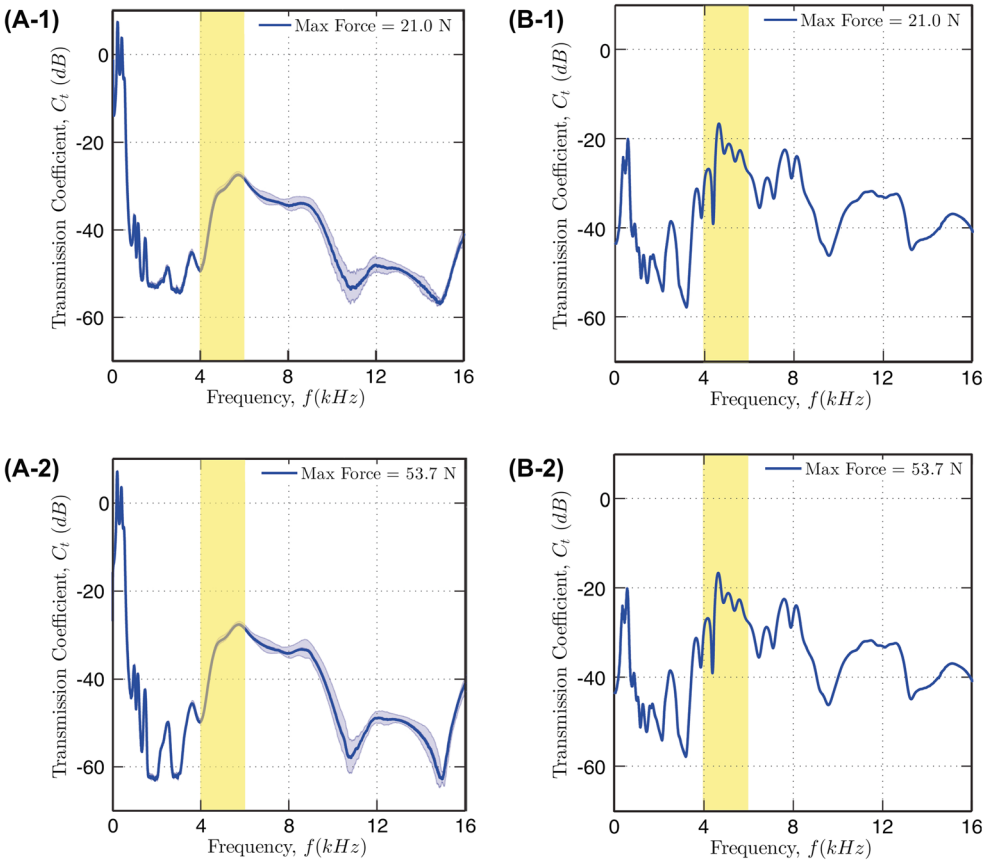

Fig. 5 Amplitude-independent transmission characteristics. **a** Transmission coefficient $C_t(\omega)$ obtained from the base excitation tests with electrodynamic shaker: (A-1) 21.0 *N*, (A-2) 53.7 *N*. Note that the shaded area denotes the standard deviation. **b** The corresponding results from the time-domain FE simulations: (B-1) 21.0 *N*, (B-2) 53.7 *N*

from the experiments. The equivalent base accelerations were obtained from the experimentally measured bottom force histories divided by the specimen mass. The acceleration histories on the FE model top were collected to calculate the transmission coefficient $C_t(\omega)$.

Figures 5B-1 and B-2 show the numerically-obtained transmission coefficient spectra $C_t(\omega)$ for the maximum force levels 21.0 *N* and 53.7 *N*, respectively. Manifesting the three low transmission frequency zones around 2 *kHz*, 10 *kHz*, and 14 *kHz*, numerical simulations are in good agreement with their experimental counterpart. From the outcomes of both experiments and simulations, we confirm that the impulse-independent transmission coefficient spectra of the considered composite specimen can be obtained by applying harmonic base excitations through a electrodynamic shaker inducing small forces.

Impact Excitation Analysis and Results

This section investigates the impulse-dependent wave transmission behavior of the considered viscoelastic phononic crystal specimen by exerting high impact excitation through SHPB apparatus. Typically, SHPB apparatus is known as a standard set-up for high strain-rate tests (e.g., up to the strain-rate of 5000/*s* or higher) [48], and it is composed of three bars: striker, input bar, and output bar (Fig. 4b). A specimen is placed between the input and output bars. By shooting the striker using a gas gun, a stress wave is created and pass through the bars and the specimen. The stress-strain response of the specimen can be calculated from the travelling waves in the bars using a simple 1-D wave propagation theory in elastic medium [48]. Recently, the idea of using SHPB apparatus for phononic band-structure study is introduced by Feng and Liu [49, 50], who have reported the stress-induced band-gap tunability of polymer-metal phononic crystals. In this section, we first discuss experimental issues in regard to the application of SHPB for viscoelastic phononic crystals, and then propose a hybrid SHPB apparatus to overcome the issues.

Considerations on SHPB Tests for Viscoelastic Phononic Crystals

Feng and Liu [49, 50] have investigated 1-D phononic crystals made of steel/epoxy and aluminum/epoxy using metallic SHPB apparatus, whose input and output bars were solid steel rods. Assuming a linearly-perturbed setting, they compared experimentally-observed phononic band-structures with numerical results obtained from elastic FE models. Note that their specimens included a viscoelastic material, epoxy [51],

whose Young's modulus (i.e., $E_{epoxy} \approx 4\ GPa$) is nearly two orders of magnitude smaller than that of the apparatus bar material (i.e., steel having $E_{steel} \approx 210\ GPa$).

The viscoelastic property of polymeric specimens and the impedance mismatch between polymeric specimens and metallic apparatus bars are critical to analyze correctly the experimental results from SHPB apparatus. In particular, several researchers have discussed solutions to address this impedance mismatch by using either polymeric bars [52, 53] or hollow metallic bars [54, 55]. Simply speaking, the impact energy to linearly deform the polymeric specimens is not sufficiently large to provide high signal-to-noise ratios on solid metallic apparatus bars. On the other hand, the impact energy which is sufficiently large to provide the desired high signal-to-noise ratios on solid metallic apparatus bars induces finite viscoelastic deformations in the polymeric specimens. Moreover, the frequency spectrum of the incident wave on the input bar is typically characterized by amplitude-drops at some frequencies, and these inherent amplitude-drops of the incident wave spectrum are primarily dependent on the striker length [56, 57]. Oversight of this limitation may result in the erroneous identification of phononic band-structure near those amplitude-drop frequencies. Thus, when SHPB apparatus is adopted for viscoelastic phononic crystal study, these critical points should be thoroughly addressed in order to properly identify phononic band-structures, i.e., wave transmission behavior.

Hybrid SHPB Configuration

We explore SHPB apparatus to investigate the impulse-dependent wave transmission behavior of viscoelastic phononic crystals. Since high impact energy should be applied to specimens, we could adopt metallic SHPB apparatus producing high signal-to-noise ratios in the incident wave. However, due to the material damping of viscoelastic layers (silicon rubber), we found that the transmitted wave strain signal on the output bar was significantly weak, causing low signal-to-noise ratios. On the other hand, polymeric SHPB apparatus could be considered to improve signal-to-noise ratios, but we also found that the force generated by the polymeric bars was insufficient to create finite deformation within the specimens while maintaining apparatus bars in their linear range to ensure 1-D elastic wave [58, 59]. In other words, in order to investigate the impulse-dependent wave transmission behavior of viscoelastic phononic crystals, we needed to have a SHPB configuration that simultaneously allows large input force to specimens and captures weak transmitted waves in the output bar. In order to overcome this challenge, we developed a *hybrid SHPB* system that consists of a metallic input bar and a polymer output bar. We adopted an aluminum input bar (type: $6061-T6$, length: 3 m, diameter: 45 mm) and a nylon output bar (type: PA-66, length: 3 m, diameter 50 mm) with aluminum strikers of various lengths. Strain gauges (EA-13-031CF-120/E from Vishay Measurements Group) were placed on each apparatus bar, and the strain signals were amplified by a signal amplifier (Vishay 2310). Then, the amplified strain signals were recorded using a DAQ system (NI PCI-6115) at a sampling rate of 2.5 MHz. In addition, the launching speed of striker on impact was recorded by a photoelectric sensor (Tritronics XP10). Additional details of the hybrid SHPB apparatus are given in Table 2.

The measured strain waves on the apparatus bars need to be transported to the specimen-bar interfaces to obtain the force and the acceleration acting on the considered specimen. The geometric and material properties of the apparatus bars affect wave propagations within the bars, whose wave characteristics can be captured by their dispersion relation. The complex-valued dispersion relation, $\kappa_{bar}(\omega) = \kappa^R_{bar}(\omega) + i\kappa^I_{bar}(\omega)$, can be experimentally obtained by performing the single-bar impact test [48, 58]. Note that κ^R_{bar} and κ^I_{bar} represent the frequency-dependent propagation and attenuation characteristics of waves in the bar, respectively. Here, we conducted a series of single-bar impact tests for the considered aluminum and nylon bars, and then experimentally obtained the phase velocity $c_{bar}(\omega) = \omega/\kappa^R_{bar}(\omega)$ and the attenuation coefficient $\kappa^I_{bar}(\omega)$. The solid lines in Fig. 6 illustrate the average value of of $c_{bar}(\omega)$ and $\kappa^I_{bar}(\omega)$ while shade areas indictate the corresponding standard deviation. Note that the red dashed lines in Fig. 6A-1/B-1 also show the Pochhammer-Chree solution [60] for the corresponding elastic counterpart. These experimentally-obtained coefficients were used throughout our study with the hybrid SHPB apparatus.

For the investigation of wave transmission behavior of specimens using SHPB, ideal incident waves would be sharp impulse time-signals, which resemble the dirac-delta function containing infinite frequency contents. Furthermore, the impulse of ideal incident waves should be high enough to excite the impulse-dependent wave characteristics of specimens. In practice, a sharp impulse signal having a short impulse duration can be archived by adopting a short striker. However, it requires very high launching speed to produce desirable amount of impulse due to its small mass, but the striker launching speed is typically limited by the specification of a given SHPB striker-launching system. On the other hand, a long striker having a large mass can generate high impulse with low launching speeds, but it suffers frequency amplitude-drops in the incident wave spectrum [56, 61, 62]. An

Table 2 Specifications of the hybrid SHPB apparatus

Parameters	Aluminum striker	Aluminum input bar	Nylon output bar
Length, L $[m]$	0.05, 0.15, 0.25	3.00	3.00
Diameter, D $[mm]$	45	45	50
Longitudinal wave speed, $c_0(\omega = 0)[m/s]$	5070	5070	1700
Mass density, $\rho[kg/m^3]$	2700	2700	1140
Distance between strain gage and specimen-bar interface, $\Delta[m]$	–	1.5	0.30

amplitude-drop represents the scarcity of some frequency contents in an incident wave. Consequently, regardless of wave characteristics of the considered specimen, the transmitted signal may lack some frequency contents near the amplitude-drops, entailing a distortion of transmission coefficients. Thus, prior to the main SHPB impact tests to be discussed in Sec. "Impact Excitation Tests with Hybrid SHPB", we conducted a series of impact tests by shooting three different strikers ($L_{str} = 50,\ 150,\ 250\ mm$) to the input bar and collected incident strain waves on the input bar. By taking the FFT of the incident strain signals, we analyzed the frequency amplitude-drops for each striker as shown in Fig. 7. The longer the striker is, the earlier the frequency amplitude-drop occurs in the frequency domain. Thus, we identified the valid frequency limit of each striker for the wave transmission coefficients of the considered specimen, i.e., up to around 20 kHz, 14 kHz, 8 kHz for $L_{str} = 50,\ 150,\ 250\ mm$, respectively.

Impact Excitation Tests with Hybrid SHPB

The impact excitation tests with the SHPB apparatus were conducted on the viscoelastic phononic crystal specimen under three different striker loading conditions: (a) 50 mm-long striker with a launching speed of 12.18 m/s, (b) 150 mm-long striker with 10.04 m/s, and (c) 250 mm-long striker with 8.42 m/s. After taking the FFT of the incident and transmitted strain signals, we calculated the input force spectrum $F(\omega)$ acting on the

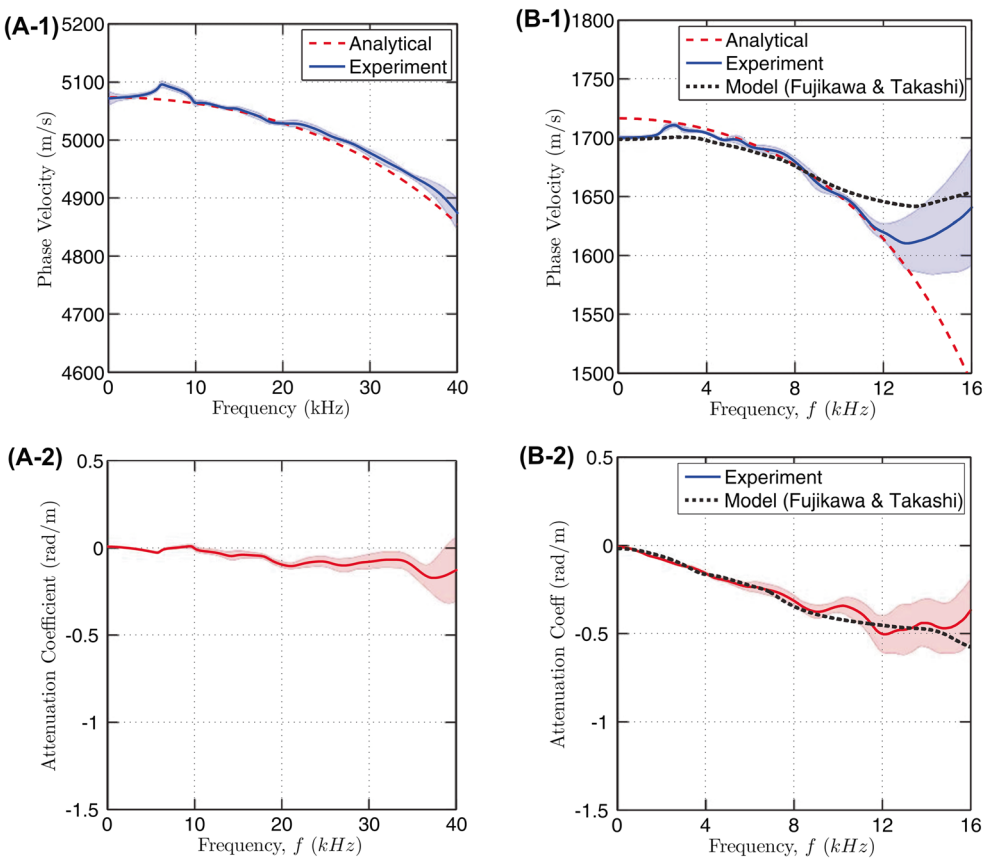

Fig. 6 Wave propagation characteristics of SHPB apparatus bars. **a** Aluminum bar: (A-1) phase velocity $c_{pl}(\omega)$, (A-2) attenuation coefficient $\kappa^I_{al}(\omega)$. **b** Nylon bar: (B-1) phase velocity $c_{pl}(\omega)$, (B-2) attenuation coefficient $\kappa^I_{ny}(\omega)$. Note that the average experimental results are denoted by the solid lines and the standard deviations are represented by the shaded areas. In addition, the dashed and the dotted lines indicate Pochhammer-Chree analytical solution and the numerically-obtained propagation coefficient from FE simulations, respectively

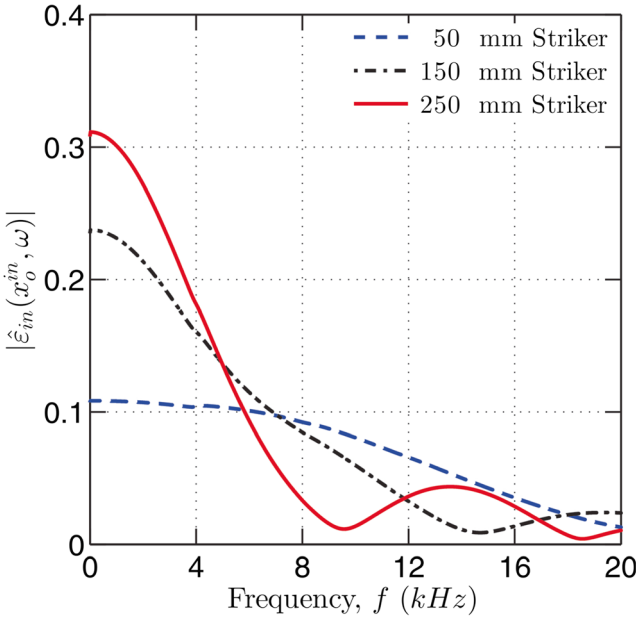

Fig. 7 Spectrum of input strain signals experimentally obtained from different striker lengths

specimen and the output acceleration spectrum $A(\omega)$ at the the interface between the specimen and the output [48]:

$$F(\omega) = \frac{s_{al}\rho_{al}\omega^2}{\kappa_{al}(\omega)^2}\hat{\varepsilon}_{inc}(\omega)e^{\kappa_{al}(\omega)^{\triangle_{al}}}, \quad A(\omega) = \frac{-i\omega^2}{\kappa_{ny}(\omega)^2}\hat{\varepsilon}_{tra}(\omega)e^{\kappa_{ny}(\omega)^{\triangle_{al}}} \tag{13}$$

where $\hat{\varepsilon}_{inc}(\omega)$ and $\hat{\varepsilon}_{tra}(\omega)$ represent the FFT of the incident and transmitted time signals measured on the apparatus bars, respectively; the subscripts *al* and *ny* represent aluminum input bar and nylon output bar, respectively; s and ρ denote the cross-sectional area and the density of the apparatus bar, respectively; $\triangle$ is the distance between the location of the strain gauge on the apparatus bar and the specimen/bar interface. Interested reader may refer to the reference [48] on the detailed formulation of (13). Then, using (11), we calculated the wave transmission coefficient $C_t(\omega)$ and summarized the results in Fig. 8a. Note that the dotted lines indicate the low-fidelity experimental results following the discussion regarding the effect of the striker length on incident waves in Sec. "Hybrid SHPB Configuration". Furthermore, by taking the inverse FFT of $F(\omega)$, we re-constructed the time-history of the input force acting on the specimen. Then, the impulse exerted to the specimen was determined by integrating the force time-history over the loading duration: (a) the impulse of 5.60 $N \cdot s$ for the 50 *mm*-long striker case, (b) 13.2 $N \cdot s$ for the 150 *mm*-long one, and (c) 18.6 $N \cdot s$ for the 250 *mm*-long one. By focusing on the solid line in Fig. 8A-1, we find two low transmission frequency zones around 2 *kHz* and 8 *kHz*, which are close to the outcome of the electrodynamic shaker tests. Due to the low signal-to-noise ratio depicted by the large standard deviation in Fig. 8A-1, the third low transmission frequency zone around 14 *kHz* was not properly identified. Interestingly, however, we find that high impulse produces a new low transmission frequency zone around 5.5 *kHz* (vertically shaded in Fig. 8A-2/3), which are neither predicted from the analytical solution from Sec. "Analytical Dispersion Relation and Transmission Coefficient" nor observed from the electrodynamic shaker tests in Sec. "Base Excitation Tests with Electrodynamic Shaker".

Time-Domain FE Simulations

For the impact excitation tests with the SHPB apparatus, we also conducted the corresponding time-domain simulations using ABAQUS/Explicit by modeling all the SHPB components (i.e., striker, input bar, output bar) as well as the specimen. All the numerical simulations were performed using a 2-D axisymmetric model with 4-node bilinear element CAX4R. Mesh sweeping sizes of 1.25 *mm* and 2.5 *mm* were adopted for the specimen and the bars, respectively. While a linear elastic material model was used for the aluminum input bar, a linear viscoelastic material model was applied for the nylon output bar. Considering the equilibrium (quasi-static) modulus $E_{ny,\infty} = 2870$ *MPa* of our nylon bar material, we adopted the scaled Prony series parameters provided by Fujikawa and Takashi [63]. After conducting an FE simulation for the single nylon bar impact test with this linear viscoelastic model, we confirmed that the numerically-obtained phase velocity and attenuation coefficient (see black dotted lines in Fig. 6B-1/2) compare well with the experimentally measured quantities. Like in the harmonic excitation simulation in Sec. "Time-Domain FE Simulations", the silicon rubber is modeled using the finite viscoelastic model described in Sec. "Material, Constitutive Model, and Specimen". In order to consider the friction between the specimen and the bars, FE simulations adopted the Coulomb friction model with a friction coefficient of $\mu_{al/al} = 1.2$ [64] and $\mu_{al/ny} = 0.1$ [65] for aluminum/aluminum and aluminum/nylon interfaces, respectively. Note that the adopted friction coefficient of aluminum-aluminum contact is greater than one and several researchers have reported that aluminum-aluminum interfaces possess a friction coefficient greater than one, ranging 1.05 to 1.4 [64, 66–69]. Based on those relevant references, we selected $\mu_{al/al} = 1.2$ [64] for the considered aluminum-aluminum interfaces modeled in the FE simulations. For each test with a different striker length (see Sec. "Impact Excitation Tests with Hybrid SHPB"), the measured launching striker speed was applied as the initial boundary condition.

Figure 8b shows the numerically obtained transmission coefficient spectra $C_t(\omega)$ for all the corresponding impact excitation tests described in Sec. "Impact Excitation Tests with

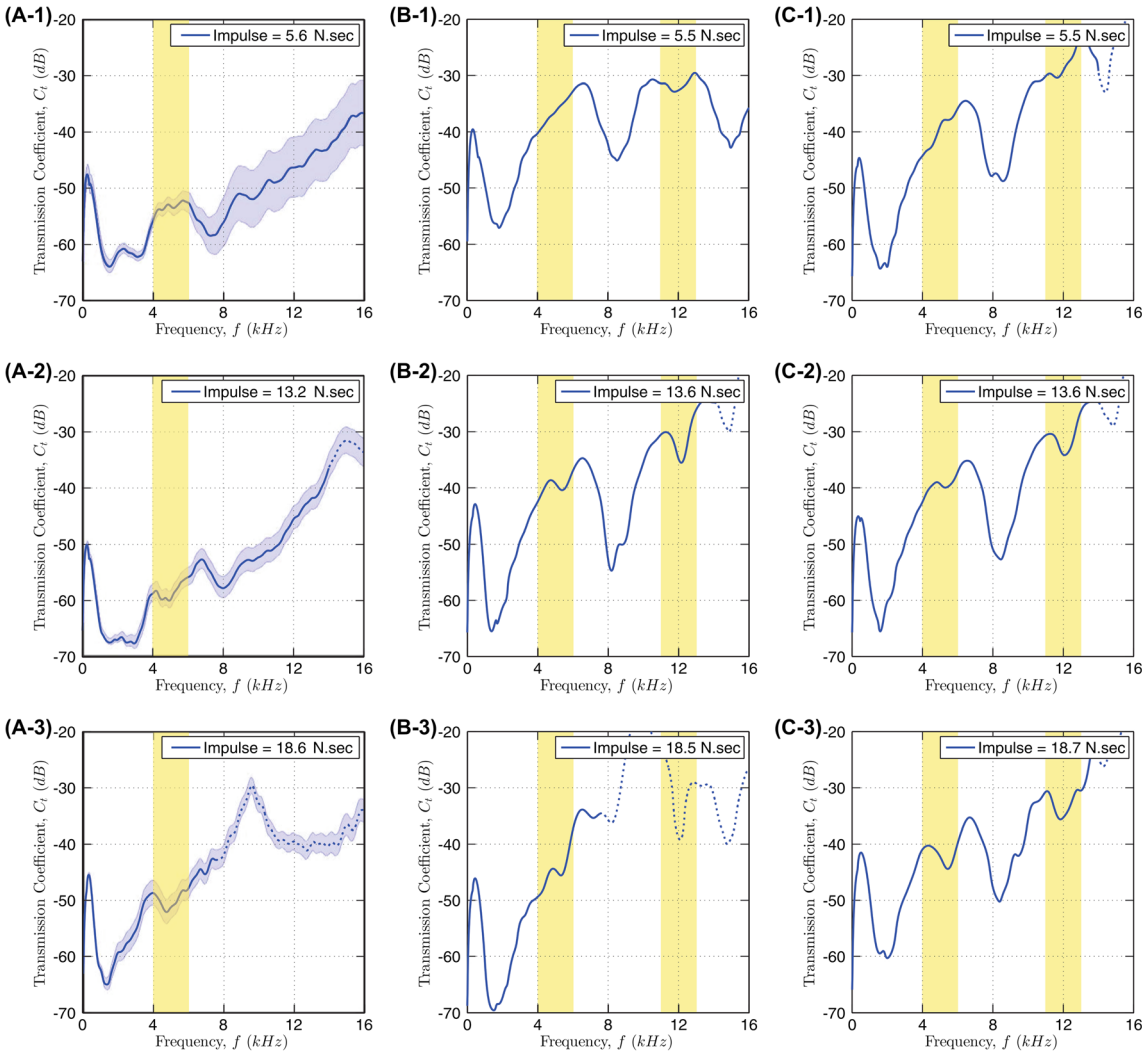

Fig. 8 Amplitude-dependent transmission characteristics obtained from SHPB setting. (A) Transmission coefficient $C_t(\omega)$ from the SHPB tests: (A-1) 50 *mm*-long striker with the impulse of 5.6 $N \cdot s$, (A-2) 150 *mm*-long striker with the impulse of 13.2 $N \cdot s$, and (A-3) 250 *mm*-long striker with the impulse of 18.6 $N \cdot s$. (B) The corresponding results from the time-domain FE simulations: (B-1) 50 *mm*-long striker with the impulse of 5.5 $N \cdot s$, (B-2) 150 *mm*-long striker with the impulse of 13.6 $N \cdot s$, and (B-3) 250 *mm*-long striker with the impulse of 18.5 $N \cdot s$. (C) The numerical results obtained from the additional time-domain FE simulations where a 150*mm*-long striker is launched for all three cases: (C-1) the impulse of 5.5 $N \cdot s$, (C-2) the impulse of 13.6 $N \cdot s$,and (C-3) the impulse of 18.7 $N \cdot s$

Hybrid SHPB". Note that the solid lines indicate the reliable experimental results following the discussion regarding the effect of the striker length on incident waves in Sec. "Hybrid SHPB Configuration". In Fig. 8B-1, we observe three distinctively low transmission frequency zones around 2 *kHz*, 8 *kHz*, and 14 *kHz*. Note that the third low transmission frequency zone around 14 *kHz* is in the vicinity of the analytical prediction (16 *kHz*) based on infinitely periodic layered composites, but is not properly identified from the experiment due to the low signal-to-noise ratio. The numerical simulation results presented in Fig. 8b also evidently show the emergence of a new impulse-dependent transmission frequency zone around 5.5 *kHz* that are observed in the experiments (Fig. 8A-2/3). In addition, Fig. 8B-1/2 show that there is another low transmission frequency zone around 12 *kHz*.

Discussion

This section first discusses the impulse-*independent* wave transmission behavior obtained from the harmonic excitation conditions. Secondly, we examine experimental and numerical results from impact excitation conditions and highlight the impulse-*dependent* wave transmission behavior of the considered viscoelastic phononic crystals.

Impulse-independent Wave Transmission Behavior from Harmonic Excitation Conditions

The analytical wave transmission coefficient spectrum in Fig. 3c was obtained by assuming steady-state harmonic wave motions in infinitely periodic viscoelastic phononic crystals.

For the electrodynamic shaker tests and the corresponding FE simulations, we considered the finite size specimen under the swept-frequency chirp signals. Despite these differences in the specimen and loading conditions, both the test and the simulation results exhibit three low-transmission frequency zones (i.e., one around 2 *kHz*, another near 10 *kHz*, and the last one around 14 *kHz* shown in Fig. 5), which are placed in the vicinity of the analytical predictions. The electrodynamic shaker tests and the corresponding FE simulations show that these three low transmission frequency zones are found to be independent of the harmonic base excitation force levels applied by the electrodynamic shaker.

In order to understand better the results of the electrodynamic shaker tests compared to those of the SHPB impact tests, we also considered the energy-equivalent conversion of a swept-frequency chirp signal into a pulse signal. Consider a unit-amplitude swept-frequency chirp signal having a time duration T_c, a linear frequency bandwidth B_c, a starting frequency f_c, and the linear rate of frequency change $k_c = B_c/T_c$. For this unit-amplitude chirp signal, Cook and Klauder [70, 71] provide a closed-form expression for an artificial energy-equivalent pulse signal $p_c(t)$:

$$p_c(t) = \left|\sqrt{iB_cT_c}\,\frac{\sin(\pi B_c t)}{\pi B_c t}\,e^{i2\pi\left(f_c t - k_c t^2/2\right)}\right| \tag{14}$$

whose central peak pulse has the amplitude of $\sqrt{B_cT_c}$ and the time duration of $2/B_c$. Note that the converted pulse signal in (14) is related to an exponentially-decaying sinc function in time domain, and the energy stored in the signal mainly resides within the central peak pulse [71]. Thus, we obtained the energy-equivalent pulse force time-signal by multiplying (14) with the average of each swept-frequency chirp force signal, and then calculated the impulse taking the time-integration. Based on this procedure, we find that the base excitation force levels of 21.0 *N* and 58.7 *N* correspond to the impulse level of 0.04 $N \cdot s$ and 0.12 $N \cdot s$, respectively. Thus, the energy-equivalent conversion of swept-frequency chirp signals reveals that the converted pulses from the electrodynamic tests are approximately two orders of magnitude smaller than the applied impulses in the SHPB impact tests.

Impulse-dependent Wave Transmission Behavior from Impact Excitation Conditions

To examine the effectiveness of the hybrid SHPB apparatus for the impulse-dependent transmission behavior study, three different levels of impulses were explored by changing the striker length and its launching speed as presented in Sec. "Impact Excitation Tests with Hybrid SHPB". At the impulse level of 5.6 $N \cdot s$, both the SHPB tests and the corresponding FE simulation (see Fig. 8A-1/B-1) show two distinctively low transmission frequency zones around 2 *kHz* and 8 *kHz*, which are close to the harmonic base excitation results. However, as the applied impulse increases, Fig. 8A/B show the appearance of a new low transmission frequency zone around 5.5 *kHz* and 12 *kHz*, which are not observed from the harmonic base excitation conditions. Recall that the reliable frequency ranges from SHPB tests are adversely affected by the striker length.

In order to assure the appearance of impulse-dependent low transmission frequency zone of the considered viscoelastic phononic crystal, we further conducted a set of additional FE simulations, which are free from the limitations relating to signal-to-noise ratios and striker launching speeds. In the additional FE simulations, we selected 150 *mm*-long aluminum striker, which provides the valid frequency limit up to 14 *kHz* based on the single-bar impact test discussed in Sec. "Hybrid SHPB Configuration". In order to achieve high impulse, we increased its launching speed, instead of using longer strikers. Striker launching speed in the FE simulations were determined to provide similar impulse magnitudes corresponding to the cases where various striker lengths were explored in Fig. 8b. For example, 150 *mm*-long striker with the launching speed of 8 *m/s* produces the impulse of 5.5 $N \cdot s$, which is close to 5.6 $N \cdot s$ generated by using 50 *mm*-long striker with the launching speed of 12.18 *m/s*. The results of the additional FE simulations are summarized in Fig. 8c, where the graphs in the same row have a similar magnitude of impulse acting on the specimen. By comparing the graphs in Fig. 8B/C side-by-side, the location of low transmission frequency zones in Fig. 8c are well compared with ones in Fig. 8b within the reliable frequency limits despite the striker length difference. This good agreement suggests that impulse serves as a proper measure to investigate the nonlinear wave transmission behavior of the considered viscoelastic phononic crystals. As the applied impulse increases, Fig. 8c clearly shows the appearance of the impulse-dependent low transmission frequency zones near 5.5 *kHz* and 12 *kHz*. In particular, note that a second impulse-dependent low transmission frequency zone around 12 *kHz* cannot be identified from the 250 *mm*-long striker.

In order to further investigate the qualitative change in transmission spectra affected by the applied impulse, we also performed a series of FE simulations by sweeping various striker launching velocities. Figure 9a shows a contour plot of transmission coefficient $C_t(\omega)$ of the considered viscoelastic phononic crystal specimen. The contour plot clearly demonstrates the evolution of transmission coefficient with respect to the applied impulse. At low impulse (e.g., 5 $N \cdot s$), there are two low transmission frequency zones around 2 *kHz* and 8 *kHz* (dark brown color). However, new low transmission frequency zones near 5.5 *kHz* and 12 *kHz* emerge around the

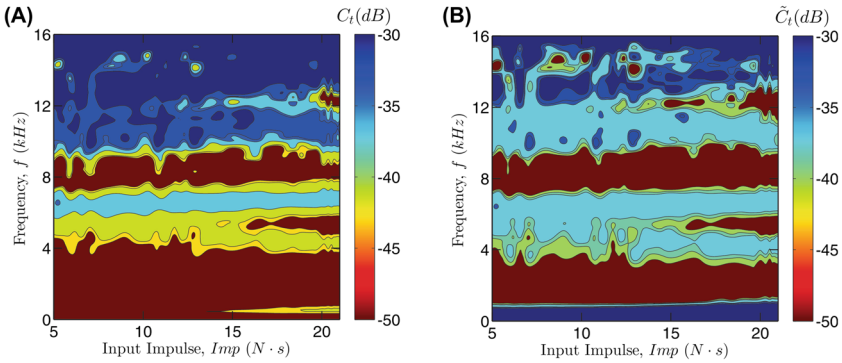

Fig. 9 Contour plots of transmission coefficient with respect to input impulse and frequency, showing the evolution of impulse-dependent wave transmission characteristics. (A) $C_t(\omega) = \|A_{out}(\omega)\|/\|F_{in}(\omega)\|$ defined in (11). (B) $\tilde{C}_t(\omega) = \|F_{out}(\omega)\| / \|F_{in}(\omega)\|$. Note that the dark brown color indicates the low transmission frequency zones

impulse of magnitude 15 $N{\cdot}s$ and 18 $N{\cdot}s$, respectively. Practically, the nonlinear wave transmission behavior can also be evaluated by using the ratio between the input force and the output force acting on the phononic crystals. So, we introduced an additional transmission coefficient spectra $\tilde{C}_t(\omega) = \|F_{out}(\omega)\| / \|F_{in}(\omega)\|$, where $\|F_{out}(\omega)\|$ and $\|F_{in}(\omega)\|$ denote the output and input force spectrum, respectively. A contour plot of force transmission coefficient $\tilde{C}_t(\omega)$ for the considered viscoelastic phononic crystal is presented in Fig. 9b. Similar to the results shown in Fig. 9a, the contour plot of $\tilde{C}_t(\omega)$ in Fig. 9b also distinctively illustrates the emergence of low transmission frequency zones at 5.5 kHz and 12 kHz as the applied impulse increases. Together with the SHPB experiments shown in Fig. 8a, these additional sets of simulation results demonstrate that the impulse-dependent wave transmission behavior can be experimentally investigated by adopting the hybrid SHPB apparatus.

Conclusions

Viscoelastic polymers are commonly employed together with metals as a constituent of phononic crystals to exploit high impedance mismatch. Recently, there has been a rising interest in the nonlinear wave transmission characteristics of phononic crystals. However, due to the inherent damping properties of viscoelastic polymers, conventional electrodynamic shakers and piezoelectric actuators are not suitable to generate sufficiently large excitation to induce nonlinear wave motion in viscoelastic phononic crystals. Thus, experimental studies have been predominantly limited to the 1-D chain of beads under impact exerted in customized impact apparatus. In this study, we propose a hybrid SHPB system and examine it as a tool to study the impulse-dependent wave characteristics of 1-D continuum viscoelastic phononic crystals. The proposed hybrid SHPB apparatus comprises an aluminum input bar and a nylon output bar in order to resolve experimental challenges related to signal-to-noise ratios and input impulse magnitudes. While the aluminum input bar allows high forces acting on the specimen, the nylon output bar improves the signal-to-noise ratio in the transmitted signals. Using the hybrid SHPB apparatus, we observed some low transmission frequency zones, which were not identified from the linearly perturbed settings such as the analytical solution and the electrodynamic shaker tests. We further conducted a series of additional FE simulations to ensure the appearance of impulse-dependent low transmission frequency zones of the considered viscoelastic phononic crystal specimen. The additional sets of simulations further illustrate the impulse-dependent evolution of transmission coefficient, and they demonstrate that the impulse-dependent wave transmission behavior can be experimentally investigated by adopting the hybrid SHPB apparatus.

SHPB apparatus is widely used as a standard set-up for high strain-rate tests of materials, and this study proposes a novel utilization such that it can also be properly used for nonlinear wave propagation characterisation of viscoelastic phononic crystals. In this study, we investigated the compression SHPB setup to evaluate wave transmission characteristics, but the experimental procedure and analysis presented in this study can also be adopted to other SHPB setups such as tension [72, 73], torsion [74, 75], and shear [76] loading conditions. Thus, this work opens a new avenue to the conventional SHPB apparatus, which can be employed to study the emerging research field of nonlinear wave characteristics of phononic crystals.

Acknowledgements The authors thank Qatar University Center for Advanced Materials facilitating the DMA tests of the considered silicon rubber. Thanks are also due to the support of the Center for Computational Research at the University at Buffalo (UB). The authors acknowledge the partial financial support through Qatar National Research Fund (QNRF) Grant No. NPRP8-1568-2-666.

Compliance with Ethical Standards

Conflict of Interests All the authors declare that there is no conflict of interest with any financial organization regarding the material discussed in the manuscript.

References

1. Kushwaha MS, Halevi P, Dobrzynski L, Djafari-Rouhani B (1993) Acoustic band structure of periodic elastic composites. Phys Rev Lett 71(13):2022–2025

2. Sigalas M, Economou E (1993) Band structure of elastic waves in two dimensional systems. Solid State Commun 86(3):141–143
3. Boechler N, Yang J, Theocharis G, Kevrekidis PG, Daraio C (2011) Tunable vibrational band gaps in one-dimensional diatomic granular crystals with three-particle unit cells. J Appl Phys 109(7): 074906
4. Bousfia A, El Boudouti EH, Djafari-Rouhani B, Bria D, Nougaoui A, Velasco VR (2001) Omnidirectional phononic reflection and selective transmission in one-dimensional acoustic layered structures. Surf Sci 482-485(2):1175–1180
5. Cao WW, Qi WK (1995) Plane wave propagation in finite composites. J Appl Phys 78(7):4627–4632
6. Manzanares-Martinez B, Sanchez-Dehesa J, Hakansson A, Cervera F, Ramos-Mendieta F (2004) Experimental evidence of omnidirectional elastic bandgap in finite one-dimensional phononic systems. Appl Phys Lett 85(1):154–156
7. Liang B, Yuan B, Cheng JC (2009) Acoustic diode: Rectification of acoustic energy flux in one-dimensional systems. Phys Rev Lett 103(10)
8. Liang B, Guo XS, Tu J, Zhang D, Cheng JC (2010) An acoustic rectifier. Nat Mater 9(12):989–992
9. Ma C, Parker RG, Yellen BB (2013) Optimization of an acoustic rectifier for unidirectional wave propagation in periodic mass-spring lattices. J Sound Vib 332(20):4876–4894
10. Saini G, Pezeril T, Torchinsky DH, Yoon J, Kooi SE, Thomas EL, Nelson KA (2011) Pulsed laser characterization of multicomponent polymer acoustic and mechanical properties in the sub-ghz regime. J Mater Res 22(3):719–723
11. Casadei F, Bertoldi K (2014) Harnessing fluid-structure interactions to design self-regulating acoustic metamaterials. J Appl Phys 115(3):034907
12. Policarpo H, Neves MM, Ribeiro AMR (2010) Dynamical response of a multi-laminated periodic bar: Analytical, numerical and experimental study. Shock Vib 17(4–5):521–535
13. Yan-Lin W, Ming-Wen C, Zi-Dong W (2011) Study on band gap structure of one dimensional phononic crystals. In: Jiang Z, Han J, Liu X (eds) New Materials and Advanced Materials, vol 152-153. Trans Tech Publications, Zurich, Switzerland, pp 1696–1699
14. Hayashi T, Morimoto Y, Serikawa M, Tokuda K, Tanaka T (1983) Experimental study on cut-off phenomenon for layered composite. Bulletin of JSME 26(211):23–29
15. Robinson CW, Leppelmeier GW (1974) Experimental verification of dispersion relations for layered composites. J Appl Mech 41(1): 89–91
16. Manktelow K, Narisetti RK, Leamy MJ, Ruzzene M (2013) Finite-element based perturbation analysis of wave propagation in nonlinear periodic structures. Mech Syst Signal Process 39(1–2):32–46
17. Narisetti RK, Ruzzene M, Leamy MJ (2011) A perturbation approach for analyzing dispersion and group velocities in two-dimensional nonlinear periodic lattices. J Vib Acoust 133(6): 061020
18. Narisetti RK, Ruzzene M, Leamy MJ (2012) Study of wave propagation in strongly nonlinear periodic lattices using a harmonic balance approach. Wave Motion 49(2):394–410
19. Ahsan Z, Jayaprakash KR (2016) Evolution of a primary pulse in the granular dimers mounted on a linear elastic foundation: an analytical and numerical study. Phys Rev E 94(4):043001
20. Ganesh R, Gonella S (2014) Invariants of nonlinearity in the phononic characteristics of granular chains. Phys Rev E 90(2): 023205
21. Daraio C, Nesterenko V, Herbold E, Jin S (2005) Strongly nonlinear waves in a chain of teflon beads. Phys Rev E 72(1):016603
22. Daraio C, Nesterenko V, Herbold E, Jin S (2006) Tunability of solitary wave properties in one-dimensional strongly nonlinear phononic crystals. Phys Rev E 73(2, 2):026610
23. Herbold EB, Kim J, Nesterenko VF, Wang SY, Daraio C (2009) Pulse propagation in a linear and nonlinear diatomic periodic chain: effects of acoustic frequency band-gap. Acta Mech 205(1–4):85–103
24. Yang J, Daraio C (2013) Frequency- and amplitude-dependent transmission of stress waves in curved one-dimensional granular crystals composed of diatomic particles. Exp Mech 53(3):469–483
25. Marechal P, Lenoir O, Khaled A, MEC EK, Chenouni D (2014) Viscoelasticity effect on a periodic plane medium immersed in water. Acta Acustica united with Acustica 100(6):1036–1043
26. Mukherjee S, Lee E (1978) Dispersion relations and mode shapes for waves in laminated viscoelastic composites by variational methods. Int J Solids Struct 14(1):1–13
27. Babaee S, Wang P, Bertoldi K (2015) Three-dimensional adaptive soft phononic crystals. J Appl Phys 117(24):244903
28. Mousanezhad D, Babaee S, Ghosh R, Mahdi E, Bertoldi K, Vaziri A (2015) Honeycomb phononic crystals with self-similar hierarchy. Phys Rev B 92(10):104304
29. Bergstrom J, Boyce M (1998) Constitutive modeling of the large strain time-dependent behavior of elastomers. Journal of the Mechanics and Physics of Solids 46:931–954
30. Shim JS, Mohr D (2011) Rate dependent finite strain constitutive model of polyurea. Int J Plast 27:868–886
31. Yeoh O (1993) Some forms of the strain energy function for rubber. Rubber Chem Technol 66:754–771
32. Brinson HF, Brinson LC (2008) Polymer Engineering Science and Viscoelasticity: An Introduction. Springer Science+Business Media, New York
33. Winter HH, Mours M (2006) The cyber infrastructure initiative for rheology. Rheol Acta 45(4):331–338
34. Charalambides MN, Wanigasooriya L, Williams JG, Goh SM, Chakrabarti S (2006) Large deformation extensional rheology of bread dough. Rheol Acta 46(2):239–248
35. Miller K (1999) Constitutive model of brain tissue suitable for finite element analysis of surgical procedures. J Biomech 32(5):531–537
36. ABAQUS (2012) ABAQUS Standard Analysis User's Manual Version 6.12. Pawtuchet
37. Collet M, Ouisse M, Ruzzene M, Ichchou MN (2011) Floquet-bloch decomposition for the computation of dispersion of two-dimensional periodic, damped mechanical systems. Int J Solids Struct 48(20):2837–2848
38. Farzbod F, Leamy MJ (2011) Analysis of bloch's method in structures with energy dissipation. J Vib Acoust 133(5):051010
39. Sprik R, Wegdam GH (1998) Acoustic band gaps in composites of solids and viscous liquids. Solid State Commun 106(2):77–81
40. Zhao YP, Wei PJ (2009) The band gap of 1d viscoelastic phononic crystal. Comput Mater Sci 46(3):603–606
41. Andreassen E, Jensen JS (2013) Analysis of phononic bandgap structures with dissipation. J Vib Acoust 135(4):041015
42. Haque ABMT, Ghachi RF, Alnahhal WI, Aref A, Shim J (2018) Sagittal plane waves in infinitely periodic multilayered composites composed of alternating viscoelastic and elastic solids. J Appl Mech. https://doi.org/10.1115/1.4039039
43. Naciri T, Navi P, Granacher O (1990) On harmonic wave propagation in multilayered viscoelastic media. Int J Mech Sci 32(3):225–231
44. Tanaka K, Kon-No A (1980) Harmonic viscoelastic waves propagating normal to the layers of laminated media. Bulletin of JSME 23(181):1092–1099
45. Ashcroft NW, Mermin ND (1976) Solid State Physics. Saunders College, Philadelphia
46. Bo Y, Yingren Z, Xiud L (2015) Discussion on dynamic numerical simulation for earthquake of immersed tunnel at seabed. The Open Civil Engineering Journal 9(1):773–782

47. Mendes N, Lourenco PB (2010) Seismic assessment of masonry "gaioleiro" buildings in lisbon, portugal. J Earthq Eng 14(1):80–101
48. Shim J, Mohr D (2009) Using split hopkinson pressure bars to perform large strain compression tests on polyurea at low, intermediate and high strain rates. International Journal of Impact Engineering 36(9):1116–1127
49. Feng RX, Liu KX (2012) Tuning of band-gap of phononic crystals with initial confining pressure. Chinese Physics B 21(12):126301
50. Feng RX, Liu KX (2012) Tuning the band-gap of phononic crystals with an initial stress. Phys B Condens Matter 407(12):2032–2036
51. O'Brien D, Mather P, White S (2001) Viscoelastic properties of an epoxy resin during cure. J Compos Mater 35:883–904
52. Gary G, Klepaczko J, Zhao H (1995) Generalization of split hopkinson bar technique to use viscoelastic bars. International Journal of Impact Engineering 16:529–530
53. Wang LL, Labibes K, Azari Z, Pluvinage G (1994) Generalization of split hopkinson bar technique to use viscoelastic bars. International Journal of Impact Engineering 15(5):669–686
54. Chen W, Zhang B, Forrestal MJ (1999) A split hopkinson bar technique for low-impedance materials. Exp Mech 39(2):81–85
55. Pervin F, Chen WW (2009) Dynamic mechanical response of bovine gray matter and white matter brain tissues under compression. J Biomech 42(6):731–735
56. Ahonsi B, Harrigan JJ, Aleyaasin M (2012) On the propagation coefficient of longitudinal stress waves in viscoelastic bars. International Journal of Impact Engineering 45:39–51
57. Othman R (2014) On the use of complex young's modulus while processing polymeric kolsky hopkinson bars' experiments. International Journal of Impact Engineering 73:123–134
58. Bacon C (1998) An experimental method for considering dispersion and attenuation in a viscoelastic hopkinson bar. Exp Mech 38(4):242–249
59. Lundberg B, Blanc R (1988) Determination of mechanical material properties from the two-points response of an impacted linearly viscoelastic rod specimen. J Sound Vib 126:97–108
60. Graff KF (1991) Wave Motion in Elastic Solids. Dover Publications, New York
61. Halvorsen WG, Brown DL (1977) lmpulse technique for structural frequency response testing. Sound and Vibration 11(11):8–18
62. Wickramarachi P (2003) Effects of windowing on the spectral content of a signal. Sound and Vibration 37(1):10–11
63. Fujikawa M, Takashi M (2003) Prony series approximation with generalized maxwell model based on collocation method. Japanese Society of Experimental Mechanics 3(4):278–284
64. Nuruzzaman DM, Chowdhury MA (2012) Effect of normal load and sliding velocity on friction coefficient of aluminum sliding against different pin materials. American Journal of Materials Science 2(1):26–31
65. Kagan VA, Weitzel SP (2002) Smart structure and integrated system: reinforced nylon and aluminum self-tapping screws. International Body Engineering Conference & Exhibition and Automotive & Transportation Technology Congress, Paris
66. Avallone EA, Baumeister T III (2006) Marks' Standard Handbook for Mechanical Engineers, 11th edn. McGraw-Hill Professional Publishing, New York City
67. Bartlett BW (1944) Coefficients of friction greater than unity. Am J Phys 12(1):48
68. Booser ER (1983) CRC Handbook of Lubrication: Application and Maintenance. CRC Publications, Boca Raton
69. Moran J, Sucharitakul T (2015) Variations in dry sliding friction coefficients with velocity
70. Cook CE (1960) Pulse compression-key to more efficient radar transmission. Proceedings of the Institute of Radio Engineers 48(3):310–316
71. Klauder JR, Price AC, Darlington S, Albersheim WJ (1960) The theory and design of chirp radars. Bell Syst Tech J 39(4):745–808
72. Gerlach R, Kettenbeil C, Petrinic N (2012) A new split hopkinson tensile bar design. International Journal of Impact Engineering 50(1):63–67
73. Mohr D, Gary G (2007) M-shaped specimen for the high-strain rate tensile testing using a split hopkinson pressure bar apparatus. Exp Mech 47(5):681–692
74. Duffy J, Campbell JD, Hawley RH (1971) On the use of a torsional split hopkinson bar to study rate effects in 1100-0 aluminum. J Appl Mech 38(1):83–91
75. Xue Q, Shen LT, Bai YL (1995) A modified split hopkinson torsional bar in studying shear localization. Meas Sci Technol 6(11):1557–1565
76. Trexler MM, Lennon AM, Wickwire AC, Harrigan TP, Luong QT, Graham JL, Maisano AJ, Roberts JC, Merkle AC (2011) Verification and implementation of a modified split hopkinson pressure bar technique for characterizing biological tissue and soft biosimulant materials under dynamic shear loading. J Mech Behav Biomed Mater 4(8):1920–1928